Turbulence in pneumatic flow focusing and flow blurring regimes

Joan Rosell-Llompart[1,2,*] and Alfonso M. Gañán-Calvo[3]
[1]*Departament d'Enginyeria Química, Universitat Rovira i Virgili, 43007 Tarragona, Spain*
[2]*Institució Catalana de Recerca i Estudis Avançats, Passeïg Lluís Companys 23, 08010 Barcelona, Spain*
[3]*E.S.I, Universidad de Sevilla, Camino de los Descubrimientos s/n 41092 Sevilla, Spain*
(Received 30 March 2007; revised manuscript received 14 December 2007; published 31 March 2008)

An important paradigm in pneumatic atomization is the production of droplet sizes in the micron and submicron range, while achieving high energy efficiency by means of simple atomizer designs. Flow focusing (FF) and flow blurring (FB) [A. M. Gañán-Calvo, Appl. Phys. Lett. **86**, 214101 (2005).] are advancements toward this goal. Both FF and FB feature a fundamental macroscopic *soft* length scale, e.g., the diameter of the liquid stream formed at a discharge orifice by conversion of pressure into liquid kinetic energy. Droplet diameter distribution data compiled from many experiments reveal that turbulent flow regimes occur in both FF and FB. In FF, like in other jet-based droplet generation techniques, the jet breakup becomes asymmetric for Weber numbers over a transitional one (approximately 20 in FF), becoming turbulent through nonlinear interactions with the gas, downstream of the discharge orifice, for large enough Weber numbers. In FB, the liquid and gas phases interact inherently in a turbulent manner: air accelerates radially and implosively toward the liquid exiting a feeding tube, and mixes with it in a region immediately preceding discharge into ambient air. In our model, droplets form by the action of turbulent pressure fluctuations present in both phases, and a resulting droplet diameter distribution is obtained when coagulation and breakup events of the liquid blobs equilibrate. When the large scale of the turbulent inertial range is taken to be the fundamental *soft* scale, the model predicts a lower bound to the experimentally determined droplet volume median diameters. On the other hand, the histograms reflect the existence of additional hard length scales imposed by the atomizer outlet geometry.

DOI: 10.1103/PhysRevE.77.036321 PACS number(s): 47.55.db, 47.55.Ca, 47.55.dr

I. INTRODUCTION

A modern paradigm in liquid atomization is the production of drop sizes in the micron and submicron range, using atomizer designs that are simple, while robust and energy efficient. An added challenge needed for nanotechnology applications is the generation of uniformly sized droplets, namely, aerosols with geometric standard deviations (σ_g's) under ~1.2. Electrospray (ES), flow focusing (FF), and their combination electroflow focusing (EFF) are liquid atomization methods exceeding conventional approaches in efficiency, control, and simplicity, that can be used for producing such "uniformly sized" droplets [1–6]. σ_g's under 1.1 are attainable in electrosprays, and have recently been demonstrated in our laboratory for flow focusing atomizers manufactured in silicon [7]. All of these methods seek to *stabilize*, rather than destabilize, the liquid-gas interface, relying on cusplike interface structures, called "cone jets," which sustain a steady microjet whose diameter is much smaller than any dimension of the atomizer body. In FF, the basic geometry comprises a feeding tube for a first fluid (that we call "focused fluid") positioned in front of a discharge orifice; a second fluid (or "focusing fluid") is forced to flow coaxially with the focused fluid through the discharge orifice via a pressure drop across it.

Cone jets do not always lead to *uniformly sized* droplets by liquid atomization. In ES, monodisperse behavior is obtained when the microjet breaks up by growth of axisymmetric waves, namely, Rayleigh breakup [8]. Rosell-Llompart and Fernández de la Mora [9] have found that this "monodisperse" behavior is interrupted by a transition from monodisperse to polydisperse aerosol behavior in ES, which is triggered by the appearance of "helicoidal" motions in the jet (also referred to as "whipping," "lateral," or "kink" instabilities). Such transitions, also discussed by Tang and Gomez [10] and by Hartman *et al.* [11], have their pneumatic counterpart in FF and even in EFF, where they all occur at a transitional value of the corresponding (hydrodynamic or electrohydrodynamic) Weber number [3,4,12]. Below such transitional value, the liquid microjet breaks up by Rayleigh breakup, where we speak of the "capillary flow focusing" (CFF) regime. Above the transitional Weber value, the regime here named "turbulent flow focusing" (TFF) is encountered, in which the jet breakup is dominated by the faster growth rate of the asymmetric disturbances over that for axisymmetric ones, leading to helicoidal or lateral jet motions, and eventually turbulent jet breakup at sufficiently high Weber number.

Both CFF and TFF regimes are bounded by another regime, named "flow blurring" (FB) [13], which is characterized by the global destabilization of the cone-jet interface and a turbulent interaction between liquid and gas phases, and is encountered upon variation of a single device geometrical parameter [14], namely the distance from the exit of the feeding tube to the discharge orifice. In FB, a backflow pattern produces efficient mixing between the gas and liquid phases, and leads to energy-efficiency improvements over other atomization processes [13]. Gañán-Calvo [13] has shown that the FB regime is several times more energy efficient than FF, indeed than any pneumatic atomization

*Previously at Aradigm Corporation, Hayward, CA 94545.

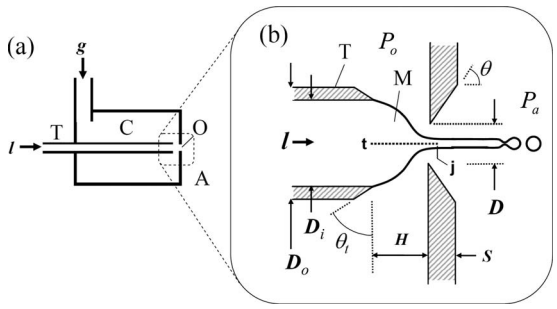

FIG. 1. Schematic of atomizer used for FF and FB. (a): Cutaway view, showing gas-pressurized chamber *C*, discharge orifice *O*, liquid feed tube *T*, and gas *g* and liquid *l* supplies. Defined in (b) are the geometrical parameters, a flow streamline running from *t* to *j*, and the liquid meniscus *M*, depicted here as a steady flow-focused cone jet (CFF regime).

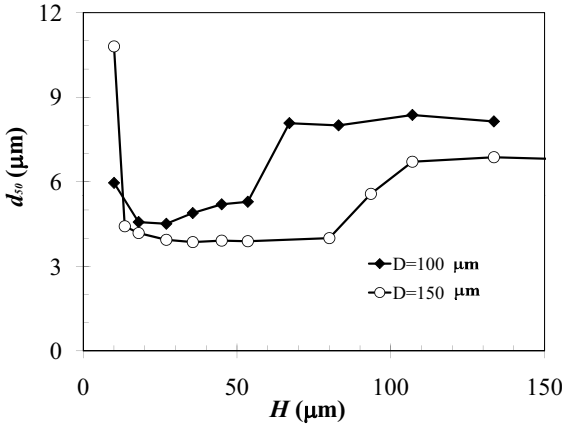

FIG. 2. Droplet median diameter of the droplet-volume distribution function (d_{50}) determined at the exit of the discharge orifice by laser diffraction sizing, vs feed-tube–to–orifice separation (H) for two devices (D in legend), whose liquid feed tube is mounted on a sliding thread allowing continuous adjustment of H. Deionized water in nitrogen. Parameters: $D_i=D$, $D_o=410$ μm, S=75 μm, $\Theta_t=0°$; $\Delta P=P_o-P_a=1$ MPa; $Q=35$ mL/h. (Adapted from Rosell and Ganan-Calvo [14].)

method known. The advantages of the turbulent regimes TFF and FB for atomic spectrometry have already been discussed by Groom *et al.* [15] and Almagro *et al.* [16].

The drop size distributions carry the signature of the liquid fragmentation process. In this paper, the aerosol drop diameter data are assembled from a large number of experiments with atomization devices designed for FF and FB. The data are analyzed in a nondimensional representation which uses a model prediction for inviscid flow-focused jets. This representation involves only fluid dynamic and liquid property information. Flow stability criteria based on the Weber number and the geometrical parameters describing the atomizer are proposed: here, owing to the relatively small viscosities of the different liquids of interest used in experiments, viscous effects seem to play a secondary role on the final aerosol features discussed herein. Pictures of the liquid ligaments produced in FB suggest an active participation of the backflow pattern in the process of liquid fragmentation, owing to an intense premixing between liquid and gas phases echoed at the discharge orifice and downstream of it: the fast gas stream violently drags and stretches the two-phase liquid-air mixture exiting the feeding tube. A theoretical model is proposed for the average drop diameter produced in FB.

II. PHASE DIAGRAM AND GOVERNING VARIABLES

A. Stability criteria

Figure 1(a) shows the elements necessary to create FF and FB flow regimes. Liquid *l* is supplied into tube *T*, and gas *g* to plenum chamber *C*, while *g* leaks out through discharge orifice *O* into ambient *A* (often, laboratory ambient). *T* and *O* are aligned and typically circular, and *T*'s inner diameter D_i is equal or larger than the orifice entrance diameter D [Fig. 1(b)]. The independent parameters controlling the atomization process are (i) the liquid properties density ρ_l, surface tension σ, and dynamic viscosity μ_l, (ii) the gas properties (under compressible or viscous conditions) heat capacity ratio γ, and dynamic viscosity μ_g, (iii) the fluid dynamic variables liquid flow rate Q, plenum pressure P_o, and ambient pressure P_a, and (iv) the geometrical parameters, primarily, inner tube diameter D_i, orifice diameter D, and tube-orifice separation H, but also the others defined in Fig. 1(b). Which flow regimes are encountered depend on criteria defined by dimensionless combinations of parameters. It has empirically been determined that flow-focused cone jets require similar values of H, D, and D_i, satisfying

$$0.6 < H/D, \quad H/D_i < 1.5, \quad D/D_i \leq 1 \quad \text{(flow focusing)}. \tag{1}$$

The upper limit on H/D_i is necessary for initiation and maintenance of stable flow, while the lower limit on H/D prevents transitioning to the FB regime [14,17].

The existence criterion for FB can be represented as

$$H/D_{\min} < H/D < H/D_{crit} \quad \text{(flow blurring)}. \tag{2}$$

Both $H/D_{\min}$ and H/D_{crit} depend somewhat on operating conditions (P_o, P_a, and Q) as well as on geometrical dimensions and mechanical tolerances, but such dependencies have not yet been systematically studied.

Figure 2 shows the FF-FB transition for devices which had a freely adjustable H distance. The sudden change in drop diameter is associated to such transition, and is found at $H/D_{crit} \approx 0.6$ or 0.65 for these orifice sizes and operating conditions. Below this value (FB), the median drop diameter stays approximately constant, until an $H/D_{\min}$ is reached, at which fine atomization is lost since the gas flow becomes too throttled. In our experiments, $H/D_{\min}$ is often around 0.1, but smaller $H/D_{\min}$ values are attainable for larger orifice diameters. In fact, we have observed $H/D_{\min}$ as small as 0.01 for a very large orifice ($D=10$ mm), which points to a clear dependence of this parameter on the thickness of gas boundary layers at the orifice vicinity. Therefore $H/D_{\min}$ ought to depend on the Reynolds number of the imploding gas stream $\mathrm{Re}_H \equiv H(\rho_{g,o}\Delta P)^{1/2}/\mu_{g,o}$ (where $\rho_{g,o}$ and $\mu_{g,o}$ are the gas

density and viscosity, taken at stagnation conditions, and $\Delta P = P_o - P_a$). In other words, at $H/D \leq H/D_{\min}$, the gas flow boundary layer thickness at the orifice and feeding tube edges is no longer thin compared to H. Figure 2 is similar to some of the runs in Fig. 5 of Groom *et al.* [15], except that their H/D_{crit}'s were smaller: between 0.3 and 0.4.

In FF, we can distinguish various flow regimes, depending on how the two streams (liquid jet and co-flowing gas streams) interact, leading to different breakup patterns of the liquid jet. The classical description of this interaction is given in terms of the Weber (We) and the Ohnesorge (Oh) numbers [18,19]:

$$\mathrm{We} = \frac{\rho_g u_g^2}{2\sigma/d_j}, \tag{3}$$

$$\mathrm{Oh} = \frac{\mu_l}{(\rho_l \sigma d_j)^{1/2}}. \tag{4}$$

Here, ρ_g and u_g are the density and velocity of the gas stream in the region of jet breakup (outside of the viscous boundary layer adjacent to the jet), and d_j is the jet diameter. At this point, it is important to mention that the jet diameter variations in the axial direction owing to different factors (viscous interaction with the co-flowing and ambient fluid, instabilities, etc.) can make these numbers difficult to quantify. It is then very useful to introduce alternative definitions using the scaling law given in [3] for d_j in terms of operating parameters, i.e.,

$$\mathrm{We} \equiv \left(\frac{8}{\pi^2}\right)^{1/4} \left(\frac{\rho_l Q^2 \Delta P^3}{\sigma^4}\right)^{1/4}, \tag{5}$$

$$\mathrm{Oh} \equiv \left(\frac{\pi^2}{8}\right)^{1/8} \left(\frac{\mu_l^8 \Delta P}{\sigma^4 \rho_l^5 Q^2}\right)^{1/8}. \tag{6}$$

We have used these definitions in all subsequent representations wherever the Weber and Ohnesorge numbers are used.

Because typically, as in all of our data sets, Oh is low (<0.1), viscous effects are of little importance in defining the general flow pattern (regime selection by our system). However, the Ohnesorge number associated to the formation of the ultimate thin filaments during the breakup into drops ought not to be small, and is expected to play an important role in the smallest size tail [20–23]. In sum, H/D and We are the main parameters necessary, and it is useful to represent the flow regimes as regions of stability in the "phase diagram" of Fig. 3. The region corresponding to FF is formed by two FF regimes: "capillary flow focusing" (CFF) and "turbulent flow focusing" (TFF). The transition between these two modes at $\mathrm{We} \sim 20$ has been obtained from the linear stability analysis of the jet breakup in flow-focused flows [12]. Within $1 < \mathrm{We} < 20$ (CFF), the liquid jet breaks up by growth of axisymmetric-capillary perturbations (Rayleigh instability). For We exceeding 20 (TFF), the growth of hydrodynamic disturbances (both axisymmetric and nonaxisymmetric) predominates over that of axisymmetric-capillary ones. Within an intermediate "transitional" range $20 < \mathrm{We} \lesssim 50$, the nonaxisymmetric *helicoidal* jet motions predicted by theory can be observed experimentally. However, as We is increased further, the ever larger amplitude of the off-axis excursions of the liquid jet intensify the interactions with the surrounding gas stream, resulting in the stretching of the liquid into long filaments. And, when $\mathrm{We} \gg 50$, this interaction and the jet breakup become *fully turbulent* [22].

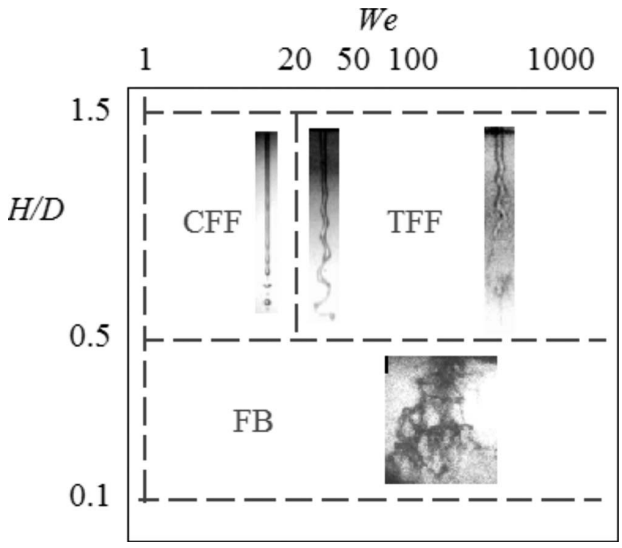

FIG. 3. Phase diagram in nozzle-configuration (H/D) and Weber (We) plane, with accompanying photographs of the liquid stream immediately after exiting O. CFF=capillary flow focusing; TFF=turbulent flow focusing; FB=flow blurring. Within TFF, as We is increased, a transition from helicoidal to fully turbulent jet motions are observed (helicoidal modes predominate between We ~ 20 and ~ 50). Photographs for capillary and helicoidal motion adapted from [12]. In this representation, the definitions (5) and (6) show their usefulness, particularly in the FB regime where no steady jet even exists.

The geometry of the exit orifice also plays a role in stability of cone jets (FF), with divergent and cylindrical orifices presumably favoring the conical meniscus geometry since the region where the gas stream is fast is confined to the vicinity of the discharge orifice, and the pressure gradient is very steep. Convergent geometries, such as employed in Lefebvre's plain jet airblast devices [18], should result in a decreased pressure gradient, presumably leading to instability of the meniscus since it must be more elongated and subject to a stronger interaction with the gas stream. Notwithstanding these considerations, a systematic study on the stability of flow-focused menisci leading to jetting as a function of the discharge orifice geometry, which is out of the scope of the present work, has not been performed yet.

B. Inviscid formation of FF jets

The inviscid ($\mathrm{Oh} \ll 1$) analysis of jet formation in FF streams leads to a dimensionless representation of the jet diameter d_j/d_o and the liquid flow rate Q/Q_o, which will be used to compare different data sets. In Fig. 1(b), liquid accelerates toward O, thinning out until once inside the orifice a liquid jet is formed, which exits O and subsequently breaks

TABLE I. Parameter values characterizing the geometry of the devices. (See Fig. 1 for meaning of column headings.)

	D (μm)	D_i/D	H/D	S (μm)	Θ (°)	Θ_t (°)
FF	50–200	1.5–2.5	0.5–1.5	50–75	0 and 60	30–60
FB	100–700	1	0.15–0.3	75–400	60	30–60

up into droplets. Under steady inviscid conditions, the static pressure field $p(x,y,z)$ is the *primary* cause for acceleration of the liquid [3]. Such pressure field is controlled via the gas plenum and ambient pressures (Fig. 1) and is impressed onto the liquid phase, acting like a "focusing force field," the gas being the focusing fluid and the liquid the focused fluid. A liquid can also act as focusing fluid, as shown experimentally or theoretically in [24–26] and computationally in [27,28]. For the streamline of Fig. 1(b) between locus "t" placed inside the liquid at the exit of T, and locus "j" inside the liquid jet, Bernoulli's equation for steady flow reads

$$p_t + \frac{1}{2}\rho_l u_t^2 = p_j + \frac{1}{2}\rho_l u_j^2, \tag{7}$$

where p is static pressure, u is local speed, and indices t, j describe locations t and j. Locus j is taken where the gas flow attains a minimum waist, or vena contracta (where, in subsonic flow, the local gas pressure is approximately equal to ambient pressure P_a). Approximations are made on account of the jet's thinness relative to D_i: (i) neglect of term $\rho_l u_t^2$ against $\rho_l u_j^2$ (since $u_t \ll u_j$); (ii) substitution of p_t (pressure at locus t) by P_o (stagnation pressure in the plenum), which is equivalent to neglect of capillary tension at t since $D_i \gg d_j$; (iii) substitution of p_j by $P_a + 2\sigma/d_j$ (gas pressure at orifice throat P_a plus the augmentation due to capillary tension). Taking these into account yields

$$\Delta P = \frac{1}{2}\rho_l u_j^2 + \frac{2\sigma}{d_j}. \tag{8}$$

Here σ is the liquid surface tension, and $\Delta P = P_o - P_a$ is the pressure drop as the gas accelerates from stagnation conditions to the discharge region. Because the first term in this equation typically dominates over the capillary term, Bernoulli's equation for the gas taken between the plenum stagnation region to the jet region $\Delta P = 1/2\,\rho_g u_g^2$ implies that the gas is several tens of times faster than the liquid $[u_g/u_l \sim (\rho_l/\rho_g)^{1/2}]$. In spite of this velocity difference, jet slenderness and viscous diffusion from the surface (transversal viscous relaxation) suffice to make the axial jet velocity profile nearly uniform along the radial direction [3]. Thus u_j is very approximately given by Q divided by the jet's cross sectional area $\pi d_j^2/4$ in most applications where thin jets are involved. Introducing characteristic dimensions d_o and Q_o defined as

$$d_o \equiv \sigma/\Delta P, \quad Q_o \equiv \left(\frac{\sigma^4}{\rho_l \Delta P^3}\right)^{1/2}, \tag{9}$$

where d_o and Q_o are of the order of the minimum attainable diameter and flow rate, respectively [3], one can reduce Eq. (8) to a fourth-order polynomial:

$$1 = \frac{8}{\pi^2}\left(\frac{Q}{Q_o}\right)^2 \cdot \left(\frac{d_o}{d_j}\right)^4 + 2\frac{d_o}{d_j} \Rightarrow \left(\frac{d_j/d_o}{(Q/Q_o)^{1/2}}\right)^4 - 2\left(\frac{d_j/d_o}{(Q/Q_o)^{1/2}}\right)^3\left(\frac{Q_o}{Q}\right)^{1/2} - \frac{8}{\pi^2} = 0. \tag{10}$$

(10)This equation can be solved exactly for $x \equiv (d_j/d_o)/(Q/Q_o)^{1/2}$. For simplicity, however, taking the zero and first orders of a series expansion of the solution in terms of $(Q_o/Q)^{1/2}$, one has

$$x = \left(\frac{8}{\pi^2}\right)^{1/4} + \frac{1}{2}\left(\frac{Q_o}{Q}\right)^{1/2} + O\left(\frac{Q_o}{Q}\right). \tag{11}$$

In conclusion, with this approximation, one can express the jet diameter as

$$d_j \cong \left(\frac{8\rho_l}{\pi^2 \Delta P}\right)^{1/4} Q^{1/2} + \frac{\sigma}{2\Delta P}, \tag{12}$$

or, in nondimensional form, using definition (5),

$$\frac{d_j}{d_o} \cong \left(\frac{8}{\pi^2}\right)^{1/4}\left(\frac{Q}{Q_o}\right)^{1/2} + \frac{1}{2} = \mathrm{We} + \frac{1}{2}. \tag{13}$$

Expression (13) agrees with published data [3] on jet diameter for values of Q/Q_o ranging from 4 to 2.5×10^4. Finally, the jet diameter is found to be independent of the geometrical parameters; however, their role is critical in ensuring stability through the criteria expressed in Eq. (1).

III. METHODS

A. Atomizer geometries

Table I provides the values of the device dimensions used.

Flow blurring. FB devices were designed having equal D_i and D. Although the H/D at which the absolute minimum droplet diameter is attained varies somewhat with We and with Re_o, robust behavior has been found for $H/D \sim 0.25$. This value was therefore adopted as our standard specification for all devices operated in the FB regime. The discharge orifice was designed to be diverging ($\Theta > 0$ in Fig. 1). While harder to manufacture than cylindrical holes ($\Theta = 0°$), diverging orifices combine negligible lip thickness at the orifice entrance with mechanical integrity, thus allowing unconstrained free gas expansion, as well as operation under "high" (several bar) pressure drop when combined with a sufficient plate thickness S (see Table I). Droplet size distributions in the FB regime were obtained with ten different devices characterized by $H/D < 0.35$, $D_i/D = 1$, and $D = 100$, 200, 250, 350, 400, 420, 500, 630, 660, and 700 μm.

Flow focusing. FF devices had more variation because

they are less sensitive to geometrical details. Both divergent and cylindrical orifices were studied. Since FF devices were sometimes operated at much lower pressures than FB, cylindrical orifices drilled on thin plates sufficed. Droplet diameter distributions were obtained with 15 different devices characterized by $0.5 \leq H/D \leq 1.5$, $1.5 \leq D_i/D \leq 2.5$, $0.25 < S/D < 1$, and $D=50$, 100, 150, 180, and 200 μm.

The estimated misalignment between the tube and orifice axes is less than 5% of D for FB devices, and within approximately 20% for FF devices.

B. Procedure and conditions for device operation

After applying gas flow at the desired pressure, liquid flow was supplied to the feeding tube either from a gas pressurized reservoir, or from a liquid-filled syringe controlled by a programmable syringe pump. In the droplet sizing experiments in FB regime, ΔP ranged between 70 kPa and 1 MPa, and Q between 10 and 14 000 μL/min, while in the FF regime, ΔP ranged between 5 kPa and 3 MPa, and Q between 10 and about 5800 μL/min (between about 100 and about 5800 μL/min in the TFF regime).

C. Materials

Data obtained with distilled water and filtered drinking water (labeled "water"), and ethanol 96% v/v aqueous (labeled "ethanol") will be presented. The focusing liquids used with these liquids were air, argon, and nitrogen. In addition, FB devices were tested with 2-propanol, 20% v/v ethanol in water, 5 mM NaCl in water, and a 30 mg/mL water-cromolyn (a pharmaceutical model) solution, with carbon dioxide as the focusing gas. These additional data sets confirmed the results for the "water" and "ethanol" sets, and will not be discussed, for economy of presentation.

D. Droplet diameter distributions

Different droplet sizing instruments were employed: an Aerometrics Phase Doppler Particle Analyzer (PDPA), a Malvern Mastersizer, and a Sympatec Helos/BF Magic laser diffraction system using lens R2. The droplet diameter distributions were parametrized by their volume-weighted median diameters d_{50} and their geometric standard deviation, σ_g [29]. The nozzle discharged the atomizate into ambient air. The region of aerosol sampling was located approximately 1 cm from the discharge orifice, where the gas flow had completed its work of atomization, the coagulation and breakup events had finally balanced, and the diameter distribution had relaxed to a "terminal atomized state," already in the "far-field" droplet size [30]. Sampling downstream of this region was avoided to prevent artifacts from droplet evaporation and coalescence: in tests in which the probe volume of the laser diffraction system was scanned along the spray axis, the droplet diameter mean was found to increase with the distance to the orifice, as the smallest droplets near the lower detectable value ($\sim$0.25 μm) disappeared presumably by evaporation and/or coalescence.

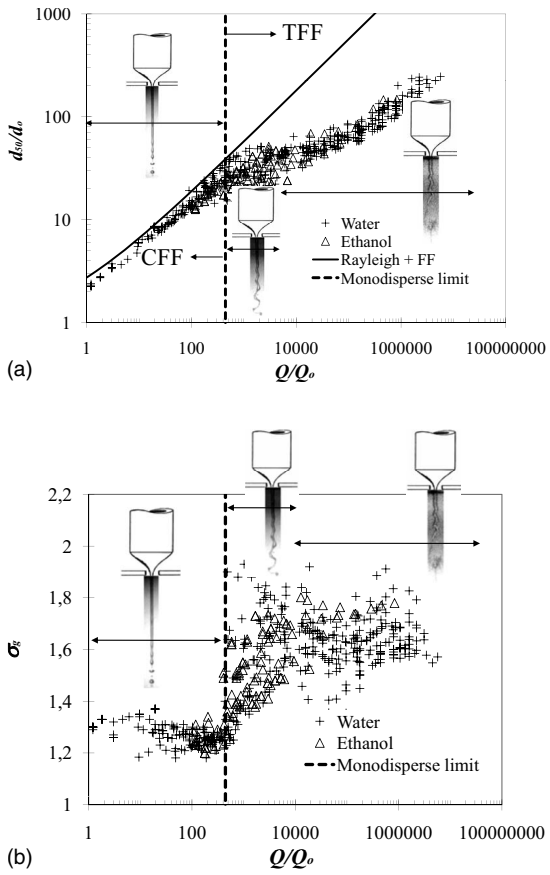

FIG. 4. Nondimensionalized droplet diameter d_{50} (a) and σ_g (b) in FF regime vs nondimensionalized liquid flow rate Q/Q_o. Experiments are with distilled water and filtered drinking water ("water"), and ethanol 96% v/v ("ethanol"). Gases: air, argon, nitrogen. Continous line "Rayleigh+FF" is Eq. (14). Dotted line represents the transition Q/Q_o (We=20) separating CFF regime (to left) from TFF regime (to right). In (a), The three inserted images are short exposure photographs of flow focused jets, showing regimes of jet breakup depending on We, from left to right: "Rayleigh" or "capillary" for We$<$20; "transitional" for 20$\leq$We; and "turbulent" for We typically exceeding 50 (first and second inserts adapted from [12]).

IV. RESULTS AND DISCUSSION

A. Flow focusing: CFF and TFF

Figure 4 assembles data from 15 FF devices with $50 \leq D \leq 200$ micrometers. Figure 4(a) shows the volume median diameter d_{50} nondimensionalized using d_o and plotted against dimensionless liquid flow rate Q/Q_o [inspired in Eqs. (12) and (9)]. Figure 4(b) shows the corresponding geometric standard deviations against Q/Q_o. Line "Rayleigh+FF" is the FF theoretical prediction of d_{50} based on Eq. (13) and inviscid Rayleigh jet breakup [31] (since drop volume is linear with jet wavelength, the volume median diameter equals $1.89d_j$ when half of the jet fragments are for shorter, and half are for longer than the Rayleigh wavelength):

$$d_{50,\text{Rayleigh+FF}}/d_o = 1.89\frac{d_j}{d_o} = 1.89\left(\text{We} + \frac{1}{2}\right), \qquad (14)$$

where d_j/d_o is from Eq. (13).

The transitional We of 20, predicted theoretically and confirmed photographically [12] to separate the low-We region for CFF from the high-We region of TFF, corresponds to $Q/Q_o=444$, and has been marked in the two graphs with a broken line labeled "Monodisperse limit". To the left of this line, experimental d_{50}'s approach the theoretical line [Fig. 4(a)] and σ_g's at about 1.2–1.3 are characteristic of "narrow" distributions [Fig. 4(b)], clearly indicating that they correspond to the CFF regime. The slight overprediction of drop diameter in this region as Q/Q_o increases may be due to the contribution of shear stresses to the shortening of the jet breakup wavelength [12]. To the right of line $Q/Q_o=444$, the drop diameter progressively departs from the "Rayleigh +FF" line [Fig. 4(a)], while the σ_g's increase suddenly [Fig. 4(b)], a situation consistent with turbulent breakup of the jet. Within this TFF region, we distinguish two behaviors for the d_{50}/d_o: (i) high scatter within range $444<Q/Q_o\lesssim 10^4$ and a zero average slope with Q/Q_o, and (ii) decreased scatter within range $Q/Q_o\gtrsim 10^4$ and an asymptotic trend with increased slope appears. We believe that these two behaviors correspond to the *transitional* and the *fully turbulent* jet behaviors described earlier. In the transitional region the subsonic and supersonic regimes coexist. The data scattering observed in this region could be explained as follows: ideally, ΔP should be the actual pressure drop experienced by the gas as it expands between plenum stagnation conditions and the region of jet breakup, whose exact location is unknown in most experiments. Naturally, the definition used for d_o does not distinguish between subsonic and supersonic conditions, and these conditions should show up in the measured droplet size. Consistently, the parametrical region where the largest dispersion in size is found [see Fig. 4(a) for Q/Q_o between about 400 and about 10^4] corresponds to the region where measurements corresponding to subsonic and supersonic conditions coexist. For Q/Q_o larger than about 10^4, all measurements correspond to supersonic conditions.

So far, this discussion has assumed perfect stability of the meniscus in the region between the feed tube exit and the orifice, in other words, existence of a steady flow-focused jet. We know from the measurements of jet diameter by Gañán-Calvo [3] that such is the case for values of Q/Q_o up to at least 2.5×10^4 (We$\simeq$160). Since this condition is at the start of the low data scatter in the high-Q/Q_o region of Fig. 4(a), it seems reasonable to extend the assumption of steady FF jets to the remaining range $Q/Q_o>2.5\times 10^4$ (to We$\sim$2000). Groom *et al.* [15], however, in a photographic study have reported the appearance of unsteadiness of the cone-jet meniscus at the reaching of a critical meniscus Weber number defined for the tube diameter D_i: $\mathrm{We}_t\equiv\Delta P D_i/\sigma$. For We_t exceeding 500, they report the "irregular distortion of the primary jet," followed by "formation of a multitude of comparatively thin and irregular streams." Unfortunately, physical similarity seems to be violated as their system has much larger geometrical dimensions (much larger dynamical forces relative to surface tension at the conical meniscus), and the liquid jet appears to be gravitationally rather than aerodynamically pulled in their system ($H\sim D\sim D_i\sim 10$ mm; assumed here to be vertically oriented). A clue hinting at gravitational pulling is the fact that the start of their jet at $\mathrm{We}_t=270$ is located very near the exit of the liquid feed tube, therefore too far away from the static pressure gradients necessary for aerodynamic focusing (which are expected to be significant only within a distance from the orifice entrance of about $D/4$). Further evidence of gravitational acceleration is gained by comparing at this condition ($\mathrm{We}_t=270$) the *local* Weber and Bond numbers at the meniscus, which is akin to comparing gravitational to inertial acceleration: From $\mathrm{We}_t=\Delta P D_i/\sigma=270$, the pressure ΔP is computed to be $\sim$2 kPa, and from it, the air speed at the edge of the water feed tube is estimated at around 11 m/s (using the potential flow approximation through a circular orifice near the axis $u_g(z)\sim(2\Delta P/\rho_g)^{0.5}/[1+(2z/D)^2]$ at $z/D=1$ where z is the axial coordinate with origin at the orifice plane). Using this speed, we find the local Weber number near the tube, where the liquid jet was formed: $\mathrm{We}_{t,local}=\rho_g u_g^2 D_i/(2\sigma)=11$. This number is comparable to—in fact, smaller than—the Bond number, which is $\mathrm{Bo}=\rho_l g D_i^2/\sigma=14$, strongly suggesting a gravitationally accelerated jet. Since Q is not reported, we cannot compare their jet diameter against our Eq. (12). Yet, by taking their jet as a flow focused jet, the ratio d_j/d_o can be estimated at $\sim$70, situating (Q/Q_o) at a value of about $\sim$5500, and their transitional condition of $\mathrm{We}_t\sim 500$ at $Q/Q_o\sim 14\,000$. This value is smaller than 2.5×10^4, the value for which we have argued earlier that FF jets are stable for our experimental Reynolds numbers (using small orifices). The possibility of meniscus destabilization cannot be ruled out in our experiments, though. In fact, it should be expected when the Reynolds number based on the orifice diameter $[\mathrm{Re}_D\equiv D(\rho_{g,o}\Delta P)^{1/2}/\mu_{g,o}]$ is raised sufficiently above 10^3, stimulated by turbulent fluctuations born in the shed vortices of the gaseous jet, and propagated upstream over the liquid-gas interface, traveling as short wavelength capillary waves. Yet, no definitive understanding can be claimed as to the critical Weber numbers at which such destabilization can occur. As a matter of fact, a Weber number defined as in [13] with the orifice diameter (instead of the jet diameter) should reflect more sharply that transition to destabilization. Unfortunately, no data supporting this statement are available with the exception of genuine FB data, where obviously the meniscus is literally disintegrated.

In summary, the pattern of behavior observed in photographic records of jets such as those of Fig. 3 is consistent with the pattern of the droplet diameter distributions of Figs. 4(a) and 4(b), namely predictable droplet diameters for We under 20 ($Q/Q_o<444$), and much smaller than predictable and high size dispersion (σ_g's) for We exceeding 20 ($Q/Q_o>444$). From a practical point of view, the TFF regime is of interest when the application tolerates certain drop size dispersion (σ_g's $\sim$1.5–1.8). Finally, Gañán-Calvo and Barrero [19] have regarded FF as fundamentally being a low-We regime in which one aims to stabilize the jet. With the hindsight gained here, FF should rather be qualified as aiming for stability of an accelerated or continuously stretched-liquid bridge (cone jet spanning between the end of the feed tube and the orifice), that leads to a jet that can display a variety of oscillatory and breakup patterns depending on We.

The scatter in d_{50}/d_o and σ_g data for $444<Q/Q_o\lesssim 10^4$ is an important facet outside our scope here, but one we want to further comment on. The scatter must arise from factors that do not scale with jet Weber number, such as orifice

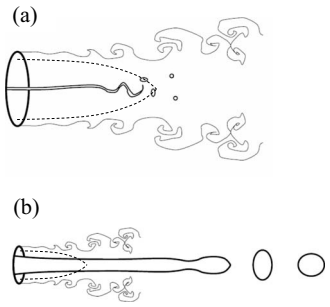

FIG. 5. Sketches of the flow-focused liquid jet exiting an orifice in the two asymptotic situations in which it is unaffected by the vortex shedding of the gas jet: (a) liquid breakup occurs within the gas jet laminar inviscid core (dotted line); (b) breakup occurs beyond the gas jet decay region.

diameter D and, as mentioned, subsonic or supersonic conditions at the discharge orifice. Any analysis based solely on Weber and Ohnesorge numbers assumes that the gas flow field becomes uniform far away from the liquid jet in the cylindrical radial direction (far field). In the laboratory, a uniform far field is approached when either (i) the jet is thin in comparison to D and is short enough to reside entirely inside the laminar inviscid core of the gas jet ("thin jet" regime) [as in Fig. 5(a)], or when (ii) the jet is thick and long, persisting beyond the gas jet turbulence decay region ("thick jet" regime) [Fig. 5(b)]. In between these two situations the ratio of d_j to D enters the picture, and one might find either increased or reduced drop size dispersion depending on which regions of the turbulent gas jet shedding frequency spectrum are picked up by the jet and amplified during breakup [19]. The data scatter may also be due in part to failing to employ in the computation of the scaling parameters d_o and Q_o the actual pressure drop from the plenum stagnation region to the actual region of jet breakup, an experimentally elusive variable. Other factors not scaling with We or Oh may influence higher moment statistics of the droplet diameter distribution, for example, upstream turbulence (as arising from Goertler vortices), swirl in the gas jet, swirl in the liquid jet, or interactions with shock waves in situations of supercritical gas flow.

B. Flow blurring

Figures 6(a) and 6(b) collect droplet volume median and σ_g data from many experiments with a variety of FB devices described in Table I. The data are normalized with d_o and Q_o to allow a comparison with the FF data of Figs. 4(a) and 4(b) for the FF regime. Such comparison reveals that significantly smaller droplets are attained by FB [Fig. 6(a)] than by FF [Fig. 4(a)] under equal conditions of flow rate, gas pressure, and liquid composition (thus equal d_o and Q_o), as well as a much gentler dependence of the drop diameter with Q/Q_o than expected for the Rayleigh+FF line. σ_g's characteristic of FB [Fig. 6(b)] spread between 1.5 and 2.1 (most between 1.8 and 2.0), being significantly higher than for the TFF regime [Fig. 4(b)].

Taken together, these differences suggest a very different liquid fragmentation mechanism from those found in the

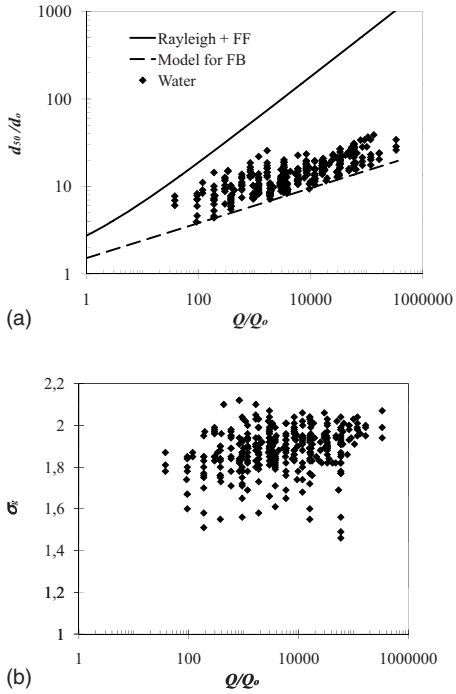

FIG. 6. Nondimensionalized (a) droplet diameter d_{50} and (b) σ_g vs Q/Q_o, over many experiments in the FB regime. Continous line "Rayleigh+FF" and dotted line "Model for FB" correspond to Eqs. (14) and (19), respectively. Liquids: distilled water, filtered drinking water. Gases: dry air, nitrogen, argon.

CFF and TFF regimes. Visualization studies were thus carried out of the region just downstream from the discharge orifice ("orifice discharge region"), and of the region immediately upstream from the orifice ("upstream region"). These results have partly been reported by Gañán-Calvo [13], who describes a backflow pattern taking place inside the liquid feeding tube, characterized by vigorous mixing between the gas and liquid phases, and ingestion of gas into the feed tube against the liquid pressure gradient. Unpublished results using high speed video in a device made with transparent walls ($D=900$ μm, $H/D\simeq 0.15$) have shown that bubbles of a broad range of sizes form inside the tube, and flow in a recirculatory pattern, with characteristic recirculation times of the order of ms, many times longer than the characteristic residence time in the orifice discharge region. Such backflow pattern develops when the gas flow becomes sufficiently *radial*, imploding at the orifice axis, and its inertia creates the gas version of a Worthington jet [32] in the backward direction, which draws liquid and gas into the feeding tube at its axis. The large speed of this gas jet is rapidly tamed by the liquid inertia, and a bubbly recirculating cavity is formed at the feeding tube exit region [13]. The photographs of Fig. 7 show the liquid and gas as they exit the orifice, and reveal that the biphasic flow density (judged from the opacity of the various regions) varies greatly both with space and time. These inhomogeneities reflect fluctuations in the liquid mass fraction caused by the presence of the largest bubbles as they exit the liquid feed tube, and which can have a diameter about 1/3 or 1/4 of the inner tube diameter. Another feature of the liquid is that rather than isolated ligaments, the liquid

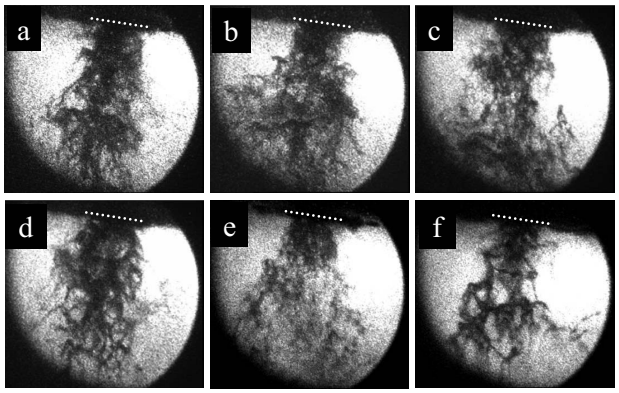

FIG. 7. Photographs showing the water-air interface in the FB regime just downstream of the discharge orifice. Conditions: (ΔP in kPa/Q in mL/min): (a)–(d) 150/3.0; (e) 150/1.5; (f) 50/0.7. Orifice exit is marked with the discontinuous white line approximately 200 μm; $D=200$ μm, $H=50$ μm; flow direction is top to bottom; exposure time=100 ns.

ligaments are interconnected, such as can be most clearly seen in Figs. 7(d) and 7(f), but also in the other panels. These ligament networks may be what remains after the collapse of liquid membranes formed between adjacent bubbles, that were originally part of the backflow stream inside the tube. One conclusion from these observations is that the backflow appears to play a *determinant* role in the atomization process, rather than a passive one. It would follow that the initial distribution of ligament sizes reflects the distribution of bubble sizes emerging from the feed tube. Ligament interconnection has previously been reported for flows mediated by liquid sheet formation [33], but not in gas-liquid co-flows. Finally, we do not find evidence of a stagnation point caused by vortex breakdown [34] in these flows, where swirl does not appear to be important.

C. Model for flow blurring

To model the situation just described, we assume that during breakup the turbulent pressure fluctuations sustained by the gas flow define an inertial subrange of isotropic turbulence [35]. Because of the short space and time scales involved, the mentioned backflow pattern may play a role in the efficient development of this subrange. Blobs of liquid of characteristic length d are viewed to detach from the liquid by the action of turbulent length scales of similar size ("eddy" of size d). This can be expressed by equating the momentum flux of a turbulent fluctuation with the capillary pressure that must be overcome for liquid blob detachment (as classically assumed in Kolmogorov's arguments):

$$\rho_g u^{*2} \sim \sigma/d. \tag{15}$$

ΔP, linearly related to the enthalpy per unit volume in the gas upstream of the atomization zone, feeds energy to these turbulent eddies. Kolmogorov's theory of isotropic turbulence teaches that the turbulent energy flux, fed at a macroscopic scale L and ultimately dissipated at the Kolmogorov scale, is of order $\sim U^3/L$, and is maintained throughout the inertial subrange so that $U^3/L \sim u^{*3}/d$, where d is the eddy size and U is provided by $\Delta P \sim \rho_g U^2$. Therefore the fraction of the total pressure drop ΔP present in eddies of size d should scale as [36,37] $(d/L)^{2/3}$

$$\frac{\rho_g u^{*2}}{\Delta P} \sim (d/L)^{2/3}. \tag{16}$$

Combining the previous two expressions and recalling Eq. (9) results in

$$d/L \sim (d_o/L)^{3/5}. \tag{17}$$

Seemingly appropriate candidates defining the largest flow scale L are either "hard" (i.e., geometrically fixed) length scales, such as the tube-orifice gap H or the orifice diameter D, or "soft" scales, such as the width of a starting liquid stream d_j (termed "soft" on account of being dependent on operating conditions). A description of L based on d_j computed using Eq. (12) with the full liquid density yields an expression for the droplet diameter that, interestingly, is cast in the same natural variables as the FF dimensionless representation:

$$d/d_o \sim (Q/Q_o)^{1/5}. \tag{18}$$

This choice of L is based on a very simple idea: if one seeks a characteristic dimension of the liquid stream with the smallest possible fluctuations in time (e.g., the smallest time dependence), the best choice falls on the area of the cross section of the discharge orifice occupied by the liquid at any instant, i.e., $A \sim (\rho_l/\Delta P)^{1/2} Q$, obtained by the same mass conservation and momentum balance considerations as those used in FF. This leads to $L \sim A^{1/2} \sim d_j$. Our proposed model does in fact relate to the experimental data over a wide number of devices and conditions, as can be seen in Fig. 6(a). In fact, the lower envelope of the data,

$$d_{50}/d_o = 1.42(Q/Q_o)^{1/5}, \tag{19}$$

is perfectly consistent with expression (18), and the participation of length scales that are longer than d_j results in larger d_{50}'s. Figure 8 illustrates such participation in the droplet diameter distributions: The droplet diameter distribution exhibits a modality of two (or higher). As Q is increased, the relative heights of the main modes varies, and a higher modality develops. The predicted diameters (d's) from Eq. (18) are close to the highest volume frequencies of the smaller-diameter peak [~0.9, 1.04, 1.24, and 1.43, respectively, for Figs. 8(a)–8(d)]. At the same time, the L's predicted from d_j's [Eq. (12)] are representative of the large diameter tail of the large diameter mode (6.6, 9.3, 14.7, 20.8, respectively). But the presence of drops larger than L reflects the existence of hard macroscopic scales, such as H or D. Theoretically, a hard macroscopic length scale would encourage the appearance of a certain mode in the histogram at a droplet diameter independent of Q, consistently with Eq. (16). Such a situation is not observed, as the diameter varies with operating conditions (both ΔP and Q), indicating the ultimate strong influence of soft scales. Finally, the possibility of a relaxation point of the droplet size distribution [30] moving downstream with Q could be a subject of subsequent work. A

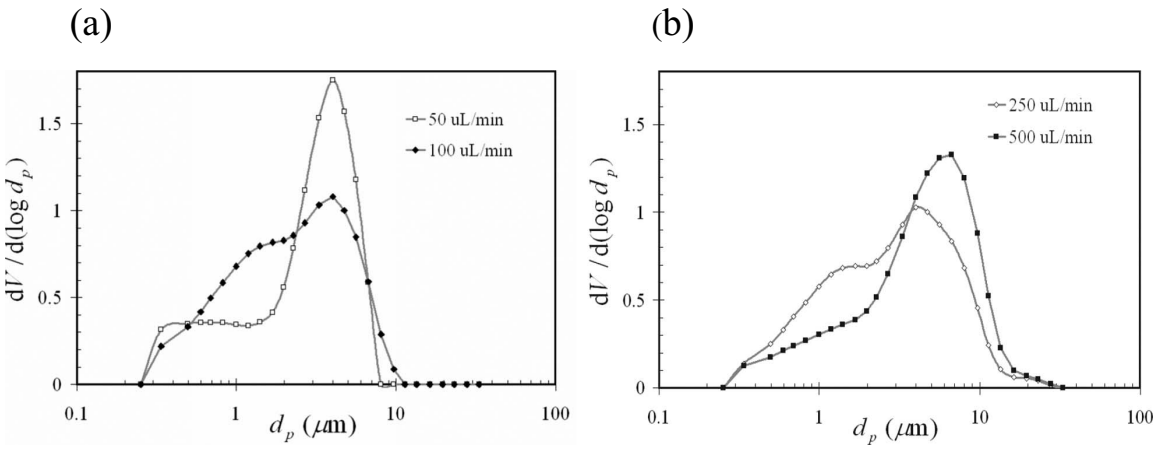

FIG. 8. Volume-frequency distributions of water-in-air aerosols by laser diffraction at $\Delta P=300$ kPa, and varying Q (legend): $dV/d\log_{10}(d_p)$ vs d_p (measured droplet diameter). Device: $D=D_i=200$ μm, $D_o=400$ μm, $H=50$ μm, $S=75$ μm, $\Theta=60°$, $\Theta_t\sim 60°$. Flow rates Q in the legends are given in μL/min.

detailed mathematical analysis of the droplet size distributions will be presented in a future publication.

V. CONCLUSIONS

The liquid aerosols generated with a great number of axisymmetric flow-focusing-type atomizers have been characterized by the median diameter (d_{50}) and geometric standard deviation (σ_g) of their droplet-volume distributions. When these statistics are represented in the nondimensional form borne out of the inviscid theory of flow focused jets, three distinct regimes can be identified: Capillary flow focusing (CFF), as well as turbulent flow focusing (TFF) and flow blurring (FB), in which the liquid phase suffers turbulent breakup. CFF is characterized by low σ_g's (between 1.2 and 1.3) and by drop diameters that are in agreement with the theoretical prediction for Rayleigh jet breakup. On the other hand, both TFF and FB result in high σ_g (1.7 and 1.9 on average, respectively), as well as in d_{50}'s that are smaller than attainable by the Rayleigh mechanism. CFF and TFF can be obtained when the tube-to-orifice separation is greater than about 0.6 orifice diameters. In this case, we speak of FF regimes, since the liquid meniscus is accelerated into a liquid jet at the discharge orifice, which subsequently breaks up into droplets. The transition from the σ_g's for CFF to those for TFF occurs rather abruptly at the jet Weber number We ~ 20, in agreement with the linear stability analysis of Gordillo *et al.* [12]. The data by Gañán-Calvo [3] suggests that the liquid meniscus in TFF remains laminar and stable for We at least up to ~ 160. It remains unclear if meniscus stability holds to higher We than this (to the highest value of Weber studied here, ~ 2000).

FB is encountered as a transition from FF when a single device parameter is varied, namely, when the separation distance between the liquid feed tube and the orifice exit (H) is reduced to a fraction of the discharge orifice diameter (D). Several devices, all with $H/D=1/4$ and with orifice and tube having equal diameter, have been studied. For fixed liquid and gas composition, as well as conditions of operation (gas pressure and liquid flow rate), the measured d_{50}'s were much smaller than by either CFF or TFF, by a factor ranging between 2 and 4, on average. Photographs of the liquid phase as it exits the discharge orifice reveal that the ligaments show interconnections, suggesting that they may be remnants of the collapse of membranes formed between the gas bubbles that participate in the backflow pattern described by Gañán-Calvo [13]. A turbulent breakup model predicts a lower bound to these d_{50}'s, when the characteristic length scale feeding turbulent energy to the inertial subrange is taken to be the theoretical flow focused diameter at the prevailing conditions.

This work has been supported by the Ministry of Education and Science (MEC) in Spain, Projects No. DPI2002-04305-C02-02 and No. DPI2004-07197, and Aradigm Corporation. J.R. wishes to acknowledge support during preparation of this paper from the European Commission (Project No. MIRG-CT-2004-511310), the Catalan Government (Project No. 2005SGR-00735), and Spanish Government MEC (Projects No. FIS2005-07194 and No. CTQ2004-22275-E-PPQ). We thank Julia Castells-Grabalós for her careful proofreading.

[1] M. Cloupeau and B. Prunet-Foch, J. Electrost. **22**, 135 (1989).
[2] O. A. Basaran, AIChE J. **48**, 1842 (2002).
[3] A. M. Gañán-Calvo, Phys. Rev. Lett. **80**, 285 (1998).
[4] A. M. Gañán-Calvo, J. M. López-Herrera, and P. Riesco-Chueca, J. Fluid Mech. **566**, 421 (2006).
[5] A. M. Gañán-Calvo, Phys. Rev. Lett. **98**, 134503 (2007).
[6] J. Fernández de la Mora, Annu. Rev. Fluid Mech. **39**, 217 (2007).
[7] A. Luque, F. A. Perdigones, J. Esteve, J. Montserrat, A. M. Gañán-Calvo, and J. M. Quero, J. Microelectromech. Syst. **16**, 1201 (2007).
[8] K. Tang and A. Gomez, Phys. Fluids **6**, 2317 (1994).
[9] J. Rosell-Llompart and J. F. de la Mora, J. Aerosol Sci. **25**, 1093 (1994).
[10] K. Tang and A. Gomez, J. Colloid Interface Sci. **184**, 500 (1996).
[11] R. P. A. Hartman, D. J. Brunner, D. M. A. Camelot, J. C. M. Marijnissen, and B. Scarlett, J. Aerosol Sci. **31**, 65 (2000).
[12] J. M. Gordillo, M. Pérez-Saborid, and A. M. Gañán-Calvo, J. Fluid Mech. **448**, 23 (2001).
[13] A. M. Gañán-Calvo, Appl. Phys. Lett. **86**, 214101 (2005).
[14] J. Rosell and A. M. Gañán-Calvo, US. Patent Publication No. US 2006/0169800, 2006.
[15] S. Groom, G. Schaldach, M. Ulmer, P. Walzel, and H. Berndt, J. Anal. At. Spectrom. **20**, 169 (2005).
[16] B. Almagro, A. M. Gañán-Calvo, H. Montserrat, and A. Canals, J. Anal. At. Spectrom. **21**, 770 (2006).
[17] J. Rosell and A. M. Gañán-Calvo, International Patent Application PCT/US00/15931, Publication No. WO 00/76673 2000.
[18] A. H. Lefevbre, *Atomization and Sprays* (Taylor & Francis, Boca Raton, 1989).
[19] A. M. Gañán-Calvo and A. Barrero, J. Aerosol Sci. **30**, 117 (1999).
[20] R. M. S. M. Schulkes, J. Fluid Mech. **309**, 277 (1996).
[21] P. K. Notz and O. A. Basaran, J. Fluid Mech. **512**, 223 (2004).
[22] E. Villermaux, P. Marmottant, and J. Duplat, Phys. Rev. Lett. **92**, 074501 (2004).
[23] G. Y. Park and G. M. Harrison, Atomization Sprays **18**, 243 (2008).
[24] S. L. Anna, N. Bontoux, and H. A. Stone, Appl. Phys. Lett. **82**, 364 (2003).
[25] L. Martín-Banderas, M. Flores-Mosquera, P. Riesco-Chueca, A. Rodríguez-Gil, A. Cebolla, S. Chávez, and A. M. Gañán-Calvo, Small **1**, 688 (2005).
[26] A. M. Gañán-Calvo and J. M. Gordillo, Phys. Rev. Lett. **87**, 274501 (2001).
[27] R. Suryo and O. A. Basaran, Phys. Fluids **18**, 082102 (2006).
[28] C. Zhou, P. Yue, and J. J. Feng, Phys. Fluids **18**, 092105 (2006).
[29] P. C. Reist, *Aerosol Science and Technology*, 2nd ed. (McGraw-Hill, New York, 1993).
[30] J. C. Lasheras, E. Villermaux, and E. J. Hopfinger, J. Fluid Mech. **357**, 351 (1998).
[31] S. Chandrasekhar, *Hydrodynamic and Hydromagnetic Stability* (Dover, New York, 1981).
[32] A. M. Worthington, *A Study of Splashes* (Longman and Green, London, 1908).
[33] N. Dombrowski and R. P. Fraser, Philos. Trans. R. Soc. London, Ser. A **247**, 101 (1954).
[34] E. C. Hopfinger and J. C. Lasheras, Phys. Fluids **8**, 1696 (1996).
[35] H. Tennekes and J. L. Lumley, *A First Course in Turbulence* (MIT Press, Cambridge, MA, 1994).
[36] T. Lemenand, D. D. Valle, Y. Zellouf, and H. Peerhossaini, Int. J. Multiphase Flow **29**, 813 (2003).
[37] G. K. Batchelor, *The Theory of Homogeneous Turbulence* (Cambridge University Press, Cambridge, UK, 1953).